

AKARI and Spinning Dust Emission

A look at microwave dust emission via the Infrared

A. Bell, T. Onaka, F. Galliano, R. Wu, Y. Doi, D. Ishihara, M. Hammonds, M. Giard

University of Tokyo, Bunkyo, Tokyo, Japan, 113-0033;

abell@astron.s.u-tokyo.ac.jp

ABSTRACT

The anomalous microwave emission (AME) still lacks a coherent explanation. Both electric dipole emission by rapidly rotating dust (“spinning dust”) and magnetic dipole emission by grains with magnetic inclusions (“magnetic dust”) have emerged as theoretically plausible explanations. We explore the spinning dust angle. Specifically, the particular scenario in which spinning polycyclic aromatic hydrocarbon molecules (PAHs) are the dominant carriers of the AME. We use AKARI/Infrared Camera (IRC), due to its thorough PAH-band coverage, to analyze 98 regions showing evidence of AME. We compare AME with infrared dust emission from 3 different approaches. The results and discussion contained here apply to a angular scales of approximately 1-degree. In general, our results support an AME-from-dust hypothesis. At 1-degree angular resolution, we do not find evidence that the AME is exclusively carried by PAHs. The correlation of far IR dust emission with AME appears to be the best predictor, with MIR/PAH emission being marginally more weakly correlated with AME. In the case of lambda Orionis, AME vs. PAH is at least as strong as AME vs. FIR. Higher resolution studies will be needed in the future to fully solve the AME mystery. re consistent with previous studies in that the AME has a clear connection to interstellar dust, but a conclusive link to any particular population of dust is unapparent.

Subject headings: AME, spinning dust, PAH bands, AKARI

1. Introduction

Since its first detection in early microwave surveys , the anomalous microwave emission/foreground (AME) has been found to be a widespread feature of the microwave Milky Way (Dickinson et al. 2013). Kogut et al. (1996); de Oliveira-Costa et al. (1997); Leitch (1998) showed that the AME correlates very well with infrared emission from dust, via COBE/DIRBE and IRAS far-IR maps. However there remains much mystery, except that the most likely source of the AME is interstellar dust (Ysard & Verstraete 2010; Tibbs et al. 2011; Hensley et al. 2016).

From the observed spatial correlation between AME and dust emerged two prevailing hypotheses:

1) Electric dipole emission by spinning small dust grains, a mechanism proposed in Erickson

(1957) and Hoyle & Wickramasinghe (1970), with further discussion in Ferrara & Dettmar (1994). Draine & Lazarian (1998b) give the earliest thorough description, with substantial updates contributed more recently by Ysard & Verstraete (2010), Ali-Haïmoud et al. (2009), Hoang et al. (2010) and several others. ? propose that such small spinning grains may consist primarily of silicates, and that observational upper-bounds of nanosilicate abundance allows for such a scenario. Dickinson et al. (2013) provide a detailed overview of AME and spinning dust literature.

2) Magnetic dipole emission, caused by thermal fluctuations in grains with magnetic inclusions, proposed by Draine & Lazarian (1999).

More recently, modeled spectra for potential candidate carriers have appeared in the literature:

PAHs, grains with magnetic inclusions (Draine & Hensley 2013; Ali-Haimoud 2014; Hoang et al. 2016).

A third, but not widely accepted, possible explanation for AME is discussed in Jones (2009). They have suggested that the emissivity of dust, in the spectral range related to AME, could contain features caused by low temperature solid-state structural transitions.

Although spinning dust need not be the only emission mechanism, the photometric signature of the AME, has so far been commonly explained via spinning dust parameters (Ysard et al. 2011; Ali-Haimoud 2010). In this paper, we explore the case that the AME signature arises from spinning dust emission. If the AME is carried by spinning dust, the carrier should be small enough that it can be rotationally excited to frequencies in the range of 10-40 GHz, and must have a permanent electric dipole. Within contemporary dust SED models, only the polycyclic aromatic hydrocarbon family of molecules (PAHs), or nanoscale amorphous carbon dust fit these criteria. Those PAHs which have a permanent electric dipole (i.e. coronulene, but not symmetric molecules like coronene), can emit rotationally. However the carrier need not be carbon-based. Indeed, Hensley & Draine (2017a) claim that AME can be explained without carbonaceous carriers, using only spinning nanosilicates.

While neither nanosilicates nor PAHs have been conclusively identified in the ISM, mid-infrared features associated with PAH-like aromatic materials have been observed. In fact, “the PAH features” are ubiquitous in the ISM (Giard et al. 1994; Onaka et al. 1996; Onaka 2000), such that the carriers must be abundant. However Andrews et al. (2015) strongly argue for the existence of a dominant “grandPAH” class, containing 20 to 30 PAH species. On the other hand, there has yet to be any detection of features related to nanosilicates. There is only an upper-bound from IRTS observations of Onaka et al. (1996) and calculations by Li & Draine (2001).

Assuming a rotational emission model, the AME signature (consistent with continuum emission having a peak around 20 to 40 GHz) implies very small oscillators (~ 10 nm). In any case, the PAH class of molecules are the only spinning dust candidate so far which show both: 1) Evidence

of abundance in the ISM at IR wavelengths, and 2) A predicted range of dipole moments (on order of 1 debye), to produce the observed AME signature (Draine & Lazarian 1998b; Lovas et al. 2005; Thorwirth et al. 2007). However, it should be noted that the current upper-bound on the abundance of nanosilicates, allows for a “spinning nanosilicate” explanation for the AME, as shown by Hensley & Draine (2017a). Due to the (apparently) continuous shape of the AME SED, a distribution of dipole moments and rotational velocities is needed, in a spinning dust scenario. Of course, the AME cannot simply be modeled by a distribution of carriers. Environmental factors must be considered.

In the spinning dust model, there are several possible excitation factors for spinning dust. While the question of whether or not such small grains would be spinning at all is a bit trivial-a case in which grains had no angular momentum would be bizarre- for the grains to have rotational velocities high enough to create the observed AME, they must be subject to strong excitation mechanisms. The dominant factors that would be giving grains their spin, are broken down by Draine (2011) into basically two categories: 1) Collisional excitation. 2) Radiative excitation, the sum of which could lead to sufficient rotational velocities for sufficiently small grains. However the extent of excitation will depend on environmental conditions, i.e. there will be more frequent encounters with ions and atoms in denser regions (so long as the density is not high enough to coagulate the small grains), and more excitation due to photon emission with increasing ISRF strength (Ali-Haimoud et al. 2009; ?). One of the strongest potential excitation mechanisms listed in Draine (2011) is that of negatively charged grains interacting with ions. Thus not only must we consider environmental factors, grain composition and size, but also the ionization state of the carriers. (For example, ionized vs. neutral PAHs.) The dependence of the observed AME on ISM density is modeled by Ali-Haimoud (2010), demonstrating that denser regions may have a stronger AME component (although it can be observationally challenging to resolve dense vs. diffuse AME producing regions.)

The overall pattern among large-scale studies seems to show that all of the dust-tracing photo-

metric bands correlate with the AME (and each other) to first-order. On an all-sky, pixel-by-pixel basis, at 1-degree angular resolution, Ysard et al. (2010) find that $12\text{ }\mu\text{m}$ emission, via IRAS, correlates slightly more strongly with AME (via WMAP) than with $100\text{ }\mu\text{m}$ emission. They also find that scaling the IR intensity by the interstellar radiation field strength (given as G_0 , a measure of ISRF relative to that of the solar neighborhood) improves both correlations. They interpret this finding as evidence that AME is related to dust, and more closely related to the small stochastically emitting dust that is traced by $12\text{ }\mu\text{m}$ emission.

However in a similar work, Hensley et al. (2016) report that the $12\text{ }\mu\text{m}$ emission (via WISE) correlates less tightly with AME than with thermal dust radiance, using the Planck Collaboration dust and AME component-separation maps (Planck Collaboration et al. 2016a). Also at odds with Ysard et al. (2010), they report that AME correlates more strongly with $12\text{ }\mu\text{m}$ intensity than with the intensity scaled by the interstellar radiation field. They interpret this as AME and PAH emission both being correlated with the total dust radiance, but that there is no preferential relationship between PAHs and the AME.

The story is no more clear when looking at the average properties of individual regions. Planck Collaboration et al. (2014c) find that among 22 high-confidence "AME regions" (galactic clouds such as the ρ Ophiuchus cloud and the Perseus molecular cloud complex) AME vs. $12\text{ }\mu\text{m}$ shows a marginally weaker correlation than AME vs. $100\text{ }\mu\text{m}$ (via IRAS). Tibbs et al. (2011) examined the AME-prominent Perseus Molecular Cloud complex, finding that while there is no clear evidence of a PAH-AME correlation, they do find a slight correlation between AME and G_0 .

In this work, we attempt to reach some stronger consensus on the large-scale AME vs. IR-dust story, keeping in mind that resolution limitations are could dilute more subtle connections between potential connections between dust IR emission and the anomalous foreground. In Section 2, we describe the all-sky surveys and component maps used in this paper. The sources range from PAH-dominated MIR bands from AKARI and IRAS to FIR and microwave-derived maps from Planck Observatory. These bands are listed in table 2, and are outlined in the following Data section. Sec-

tion 3 describes our investigation approach: looking at all-sky trends, a circular aperture photometry on a list of regions of interest, and a localized study of the AME region of largest angular size, lambda Orionis. Section 4 describes the conclusions of these 3 approaches, and compares them to previous AME vs. dust emission studies.

We utilize the newly created AKARI/IRC $9\text{ }\mu\text{m}$ all-sky map, which more completely covers PAH features than previous all-sky surveys, and has the highest fractional contribution from PAH emission, as can be seen in Fig. 2.1, assuming a PAH and grain SED model such as Draine & Li (2001). This is especially true as the ISRF intensifies, and the IRAS or WISE $12\text{ }\mu\text{m}$ bands include more continuum emission.

2. Data

This work relies completely on all-sky surveys. All of the maps utilized are photometric-band infrared maps, except for the AME data, which is an all-sky component separation analysis product, from the Planck Collaboration's efforts to separate galactic foregrounds from the CMB.

We are primarily interested in the AKARI/IRC $9\text{ }\mu\text{m}$ band's unique coverage of the PAH bands at 6.2 , 7.7 , 8.6 , and $11.2\text{ }\mu\text{m}$, and if this shows any stronger/weaker correlation with AME than the WISE or IRAS $12\text{ }\mu\text{m}$ bands. In total, we use all-sky maps from 19 photometric bands, spanning the wavelength range of $6.9\text{ }\mu\text{m}$ to $550\text{ }\mu\text{m}^{**}$

2.1. Infrared Data

The AKARI infrared space telescope revealed an entire sky of infrared light, from the mid to far infrared, via two instruments (Murakami et al. 2007) the Infrared Camera (IRC)(Onaka et al. 2007) and the Far Infrared Surveyor (FIS) (Kawada et al. 2007a).

IRC's $9\text{ }\mu\text{m}$ band all-sky map demonstrates the abundance of the PAH bands carrier in the Milky Way (Ishihara et al. 2010). Figure 2.1 shows the coverage of the MIR bands along with an example galactic cirrus SED. The $9\text{ }\mu\text{m}$ band uniquely covers major ionized PAH features at 6.2 and $7.7\text{ }\mu\text{m}$; as well as neutral PAH features at 8.6 and $11.2\text{ }\mu\text{m}$ across the entire sky (Onaka et al. 2007). The IRAS $12\text{ }\mu\text{m}$ band covers the 11.2 and $8.6\text{ }\mu\text{m}$ features, and the similarly-shaped WISE $12\text{ }\mu\text{m}$ band

covers primarily the $11.2\text{ }\mu\text{m}$ feature. According to this distribution of PAH features across the response filters, it is expected that the IRC $9\text{ }\mu\text{m}$ band is most dominated by PAH emission. Figure 2.1 shows the relative contribution of neutral PAHs vs ionized PAHs to the AKARI/IRC $9\text{ }\mu\text{m}$, IRAS $12\text{ }\mu\text{m}$ and WISE $12\text{ }\mu\text{m}$ bands, based on the DL01 dust SED model. IRC $9\text{ }\mu\text{m}$ shows a larger contribution from ionized PAHs, by about 16 percent, and a conversely smaller contribution from neutral PAHs. These relative contributions remain relatively constant out to a G_0 of about 100, with the contribution from warm dust becoming a larger factor for the IRAS $12\text{ }\mu\text{m}$ and WISE $12\text{ }\mu\text{m}$ bands. Thus, according to the DL01 template, IRC $9\text{ }\mu\text{m}$ should have the highest contribution from PAHs (especially ionized) out to extreme radiation fields. Fig. 2.1 demonstrates how the band ratios of the IRC $9\text{ }\mu\text{m}$ band vs. the other MIR bands change with different modeled PAH ionization fractions (determined using the DustEM default model template, by ?).

We utilize the most recent version of the IRC data (Ishihara, et al., in prep.) This version has had an updated model of the Zodiacial light, fitted and subtracted. The details of the improved Zodi-model, which offers an improvement over that used for the IRAS all-sky maps, are given in Kondo et al. (2016).

The AKARI Far Infrared Surveyor (FIS) gives us photometric data around the peak of the typical thermal dust SED. FIS was equipped with four wavebands: two narrow bands centered at $65\text{ }\mu\text{m}$ and at $160\text{ }\mu\text{m}$, and two wide bands at $90\text{ }\mu\text{m}$ and at $140\text{ }\mu\text{m}$. An all-sky survey was carried out at each band (Kawada et al. 2007b), and the processed maps have been publicly released (Doi et al. 2015).

The Planck Space Observatory (Planck) High Frequency Instrument (HFI) all-sky maps, spanning 100 to 857 GHz (Planck Collaboration et al. 2014a) constrain the far IR dust emissivity. This study utilizes the 857 GHz ($345\text{ }\mu\text{m}$) and 545 GHz ($550\text{ }\mu\text{m}$) bands.

Data from the Infrared Astronomical Satellite (Neugebauer et al. 1984) all-sky surveys are used to supplement the similarly-centered AKARI photometric bands. The IRAS $12\text{ }\mu\text{m}$ band is similar to the AKARI $9\text{ }\mu\text{m}$ band in terms of the sky coverage, central wavelength, and especially

in that both surveys are heavily dominated by zodiacal light. We use the Improved Reprocessing of the IRAS Surveys (IRIS) (Miville-Deschénes & Lagache 2005), which use undergone a zodiacal-light removal. The Zodiacial light model, however differs between the two bands. The IRAS Zodi-subtraction is primarily based on the Kelsall et al. (1998) model.

2.2. AME Data

We utilize the COMMANDER-Ruler AME component separation map, from the Planck Collaboration's Public Data Release 2 (hereafter, PR2). Details of the foreground contribution estimates are given in Planck Collaboration et al. (2014b). The PR2 AME map was created primarily for the purpose of isolating the CMB from galactic microwave emission. Thus we do not consider it to be a definitive data set for the absolute anomalous flux in a given pixel, but rather a rough look at the whole-sky relative variation of the AME. It is not to be taken as a perfect isolation of the AME, however it is the only all-sky estimate of the AME which incorporates the Planck data. We also quote AME estimates for 98 circular apertures, found in Planck Collaboration et al. (2014c), that were made using a more careful region-by-region component separation method at 1-degree resolution.

2.3. All-sky Data Processing

The HFI, FIS, and IRIS maps used here are downloaded from their respective online repositories, as all-sky HEALPix (Górski et al. 2005) NSIDE 2048 maps. In the case of the IRC maps, we first create HEALPix maps from the 4,857 all-sky survey tiles using the Aladin all-sky data visualization platform (Bonnarel et al. 2000). NSIDE 2048 implies an average pixel spacing of $1.7'$. The maps are then degraded to NSIDE 1024 before carrying out the Gaussian-beam smoothing to a 1-degree FWHM. Following the smoothing process, the maps are degraded once more to NSIDE 256. The value of each of the larger NSIDE 256 pixels, comes from the mean of its parent NSIDE 1024 pixels. The purpose of this processing is to ensure that all of the maps have the same resolution as the PR2 AME map.

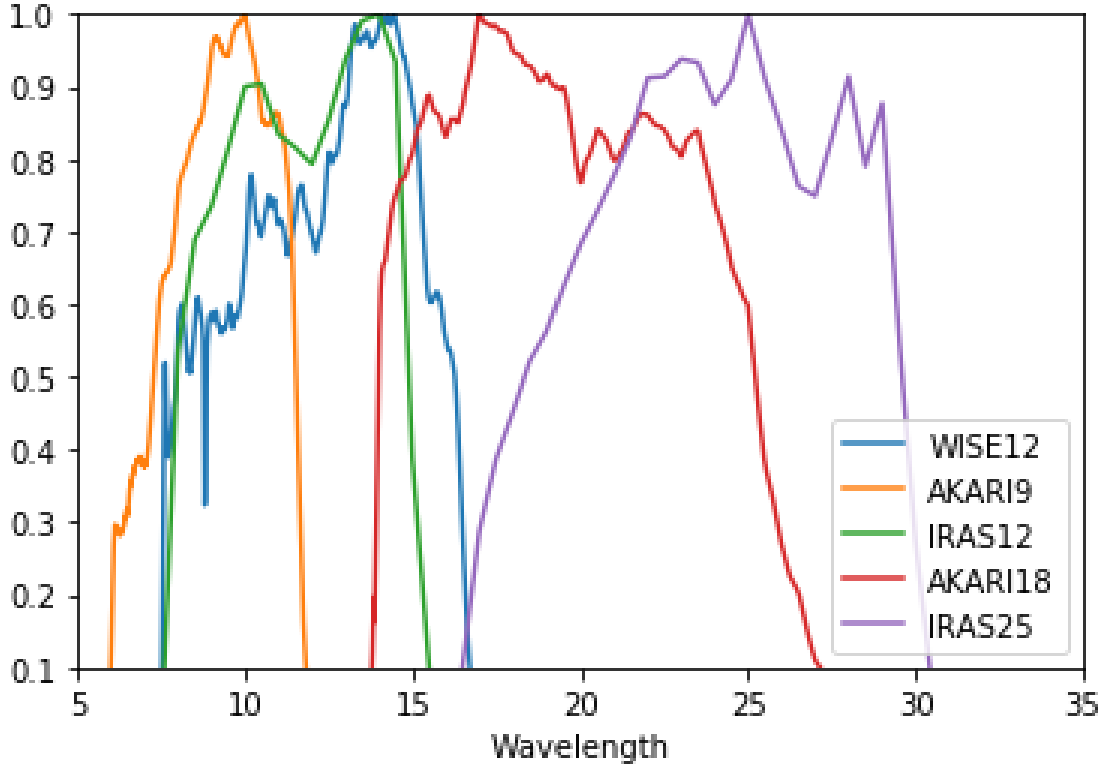


Fig. 1.— Relative spectral response curves of the MIR bands used in this study, AKARI/IRC 9 μm , IRAS 12 μm , WISE 12 μm , AKARI 18 μm , and IRAS 25 μm . AKARI/IRC 9 μm , IRAS 12 μm , WISE 12 μm bands are dominated by PAH emission (see Figure 2.1. The AKARI 18 μm , and IRAS 25 μm bands contain minimal PAH emission.

Table 1: Observational data sources used in this article

Instrument	Central Wavelength	FWHM	Uncertainty	Reference
AKARI/IRC	9 μm	~10"	<10%	(Ishihara et al. 2010)
AKARI/IRC	18 μm	~10"	<10%	"
AKARI/FIS	65 μm	63"	<10%	(Doi et al. 2015; Takita et al. 2015)
AKARI/FIS	90 μm	78"	<10%	"
AKARI/FIS	140 μm	88"	<10%	"
AKARI/FIS	160 μm	88"	<10%	"
COBE/DIRBE	12 μm			
COBE/DIRBE	25 μm			
COBE/DIRBE	60 μm			
COBE/DIRBE	100 μm			
IRAS/IRIS	12 μm	4.0'	<5.1%	(Miville-Deschénes & Lagache 2005)
IRAS/IRIS	25 μm	4.0'	<15.1%	"
IRAS/IRIS	60 μm	4.2'	<10.4%	"
IRAS/IRIS	100 μm	4.5'	<13.5%	"
Planck/HFI	345 μm	4.7'		(Planck Collaboration et al. 2014a)
Planck/HFI	550 μm	4.3'		"

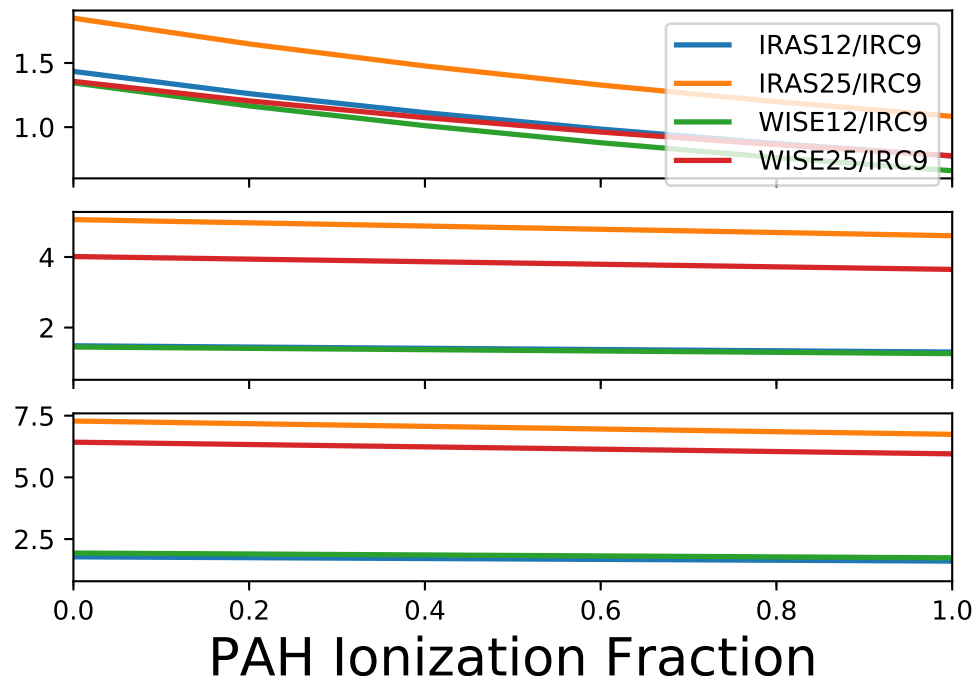


Fig. 2.— Ionization fraction of PAHs vs. band ratios of IRAS12 and 25, and WISE 12 and 25 μm bands vs. the AKARI 9 μm band, for three ISRF strengths: Top: $G_0 = 100$, Middle: $G_0 = 1000$, and Bottom: $G_0 = 10000$. These ratios are determined by assuming the SED template if ?

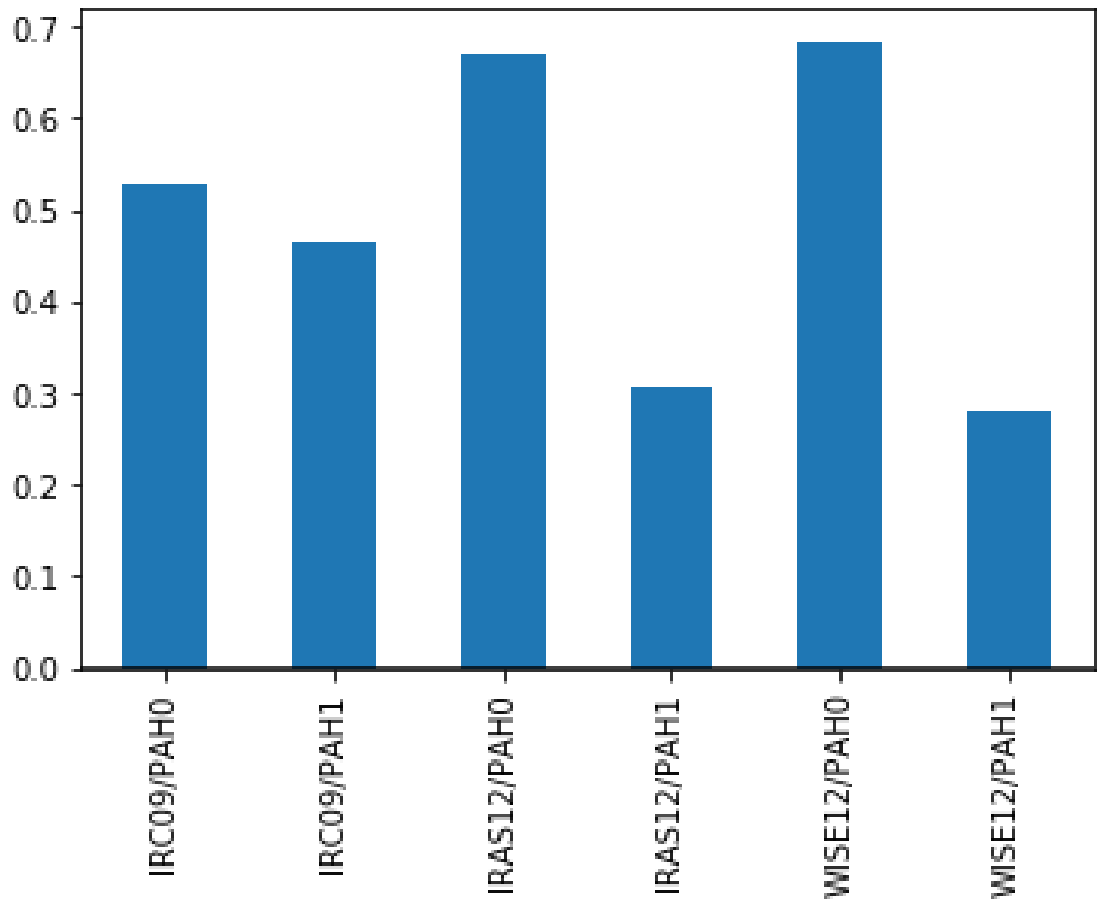


Fig. 3.— Fractional contribution of ionized vs. neutral PAH emission, based on the DL01 dust SED model at G_0 of 1. G_0 is the interstellar radiation field strength relative to that of the solar neighborhood. PAH0 and PAH1 refer to neutral and ionized PAHs.

3. Analysis

The analysis we have done so far is done from 3 perspectives, but with all 3 relying on 1-degree resolution, Planck-based AME data. 1) We start with an all-sky AME to IR comparison, looking at trends among all pixels except those within 10 degrees of the ecliptic plane. 2) Next we show a slightly more regionalized comparison, looking at the set of AME-prominent galactic clouds identified by the Planck Collaboration et al. (2014c). In that case, we try to maintain comparability between their IRAS-Planck based result, and our result which adds-in AKARI data and dust SED fitting. 3) Lastly, we highlight a particular AME-dominated region, the “Meissa ring”, otherwise known as the λ Orionis molecular ring (Maddalena 1986; Maddalena & Morris 1987).

3.1. All-sky Pixel Domain Analysis

In order to look more closely at the variations between the individual bands’ maps, we include a pixel-by-pixel analysis. Figure 3.1 shows the result of such a comparison, for each of the 19 bands sampled. The AME data comes from PR2, produced by the COMMANDER component separation method.

To keep our analysis comparable to previous works, we carry-out the analysis by excluding pixels within 10 degrees of the ecliptic plane, where the Zodi-residuals can be a problem (especially in the MIR.) The remaining pixels are divided into “high galactic latitudes” ($|l| > 10$), and “low to mid galactic latitudes” ($|l| < 10$).

We can quickly see that, for all of the bands, there is a first-order correlation between the IR with the AME. Figure 3.1 visualizes the cross-correlation matrix for each of the IR bands. The AME does not show a strong correlation with other bands at $|l| > 10$. At $|l| < 10$, the FIR bands show stronger correlation. The AKARI 9 μm bands, and the other PAH-tracing bands show a stronger correlation only relative to the bands from 18 to 60 μm . The WISE 12 μm band is shown for comparison purposes, but the version of the WISE 12 μm map used here has been released only for visualization purposes¹.

Even excluding pixels near the ecliptic plane,

and separating the sky into two b ranges, the situation is very difficult to interpret. To understand if the same pattern persists across the sky rather than presenting only for the all-sky average, we repeat the correlation analysis for b bins. For each degree of b , we cross correlate that Planck modified blackbody fitting results vs. the AME and the AKARI 9 μm intensity. (This comes with the caveat that the galactic plane is much more heavily sampled than the galactic poles.) Fig. ?? shows the results.

We do the same analysis by galactic longitude as well, also in 1-degree bins. As shown by Fig. ??, this approach produces a much more consistent result with the rank of correlation strengths remaining constant across all longitudes. There is an unexplained variation between $b = 200$ and 250.

3.2. Analysis of Planck Collaboration AME Candidate Regions

Previously, Planck Collaboration et al. (2014c) (hereafter, PCXV) identified and analyzed a list of regions where the AME appeared to stand out, relative to estimates of known microwave foregrounds. The full set includes 98 regions. While the majority of these regions showed only

$$\sigma < 5$$

AME or a high potential contribution from free-free emission, 27 showed AME at

$$\sigma > 5$$

and unlikely confusion with ultra-compact HII regions. We re-examined the full set of 98 regions, employing data from 19 photometric bands, from the AKARI, Planck, IRAS, and WISE data sets. The major goals are 1) To see how the AME to IR comparison looks with the AKARI data, and 2) To apply a dust SED fitting analysis to these regions. While tackling these goals, we attempted to keep our analysis is comparable as possible to the PCXV analysis by following their circular aperture photometry scheme. The process can be summarized as follows:

1) For each region, the total flux within a 1 degree radius circular aperture is summed.

2) A background annulus, with inner radius 80' and outer radius 100', is placed around the source

¹<https://faun.rc.fas.harvard.edu/ameisner/wssa/index.html>

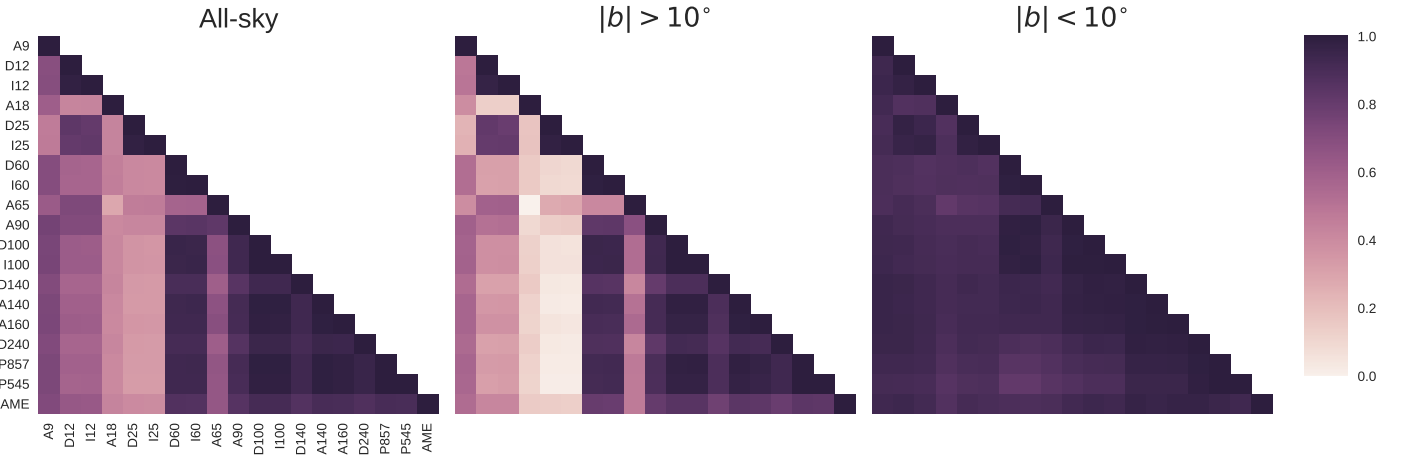


Fig. 4.— A colorized visualization of the ALL-SKY cross-correlation matrix for the 19 infrared bands sampled and the AME map. The color-scale indicates the Spearman rank. These results are based on the full sky (but omitting pixels within 10 degrees of the ecliptic plane) cross correlation of each band vs. every other band and the AME map.

aperture. The median value of pixels inside the annulus is taken, and then scaled up to solid angle of the central source aperture. This is used as background level, to be subtracted from the source flux. This is the same photometry strategy employed in Planck Collaboration et al. (2014c) to optimize source-background separation.

3) The noise level is estimated from the standard deviation of the background annulus pixels (estimating the noise level of large regions such as these is not a straightforward task.) We should note that for a few regions, the photometry done here using the PR2 map, and the photometry done on the same regions in PCXV, show discrepancies in the total flux measured (see Figure 3.2). These discrepancies do not alter our overall conclusions. The difference likely comes from the different AME separation approaches of the PR2 AME map and the region-by-region component separation of PCXV.

Once photometry results were gathered for all of the 98 regions, we performed a full dust SED fitting according to the Galliano et al. (2011) dust model. We used a mixture of amorphous carbon and silicate dust. Indeed, this dust mixture is more emissive than the standard silicate-graphite (Draine & Li 2007), by a factor of 2-3. As was shown by Herschel, in the LMC (Galliano et al. 2011), and by Planck, in the Milky Way (Planck

Collaboration et al. 2016c), this increase of emissivity is necessary to have a proper fit of the sub-mm emission. We assume that the radiation field heating this dust mixture is the Galactic ISRF (Mathis et al. 1983), scaled by a factor U . We also assume, following Dale et al. (2001), that the dust is exposed to a distribution of starlight intensity, distributed as:

$$dM_{dust} \propto U^{-\alpha} dU \quad (1)$$

between U_{min} and U_{max} , where U_{min} , U_{max} and α are free parameters. An old stellar population template (PEGASE; (Fioc & Rocca-Volmerange 1997)) is added to this SED in order to model the near-IR emission. The emission of this dust model is demonstrated in Fig. 3.2. We perform a simple least-squares analysis. For the vast majority of the samples, the fits are reasonable, with the χ^2 distribution shown in Fig. 3.2. The results of the SED fitting vs. the AME are shown in Fig. 3.2. Two comparisons are shown - AME vs. PAH mass and AME vs. total dust mass, for two different AME data sets. The AME (PR2) data indicates the results of this work (our own photometry on the publicly available Planck 'COMMANDER' algorithm based AME map.) The AME (PCXV) plots, on the bottom, indicate that the AME flux values are those quoted from

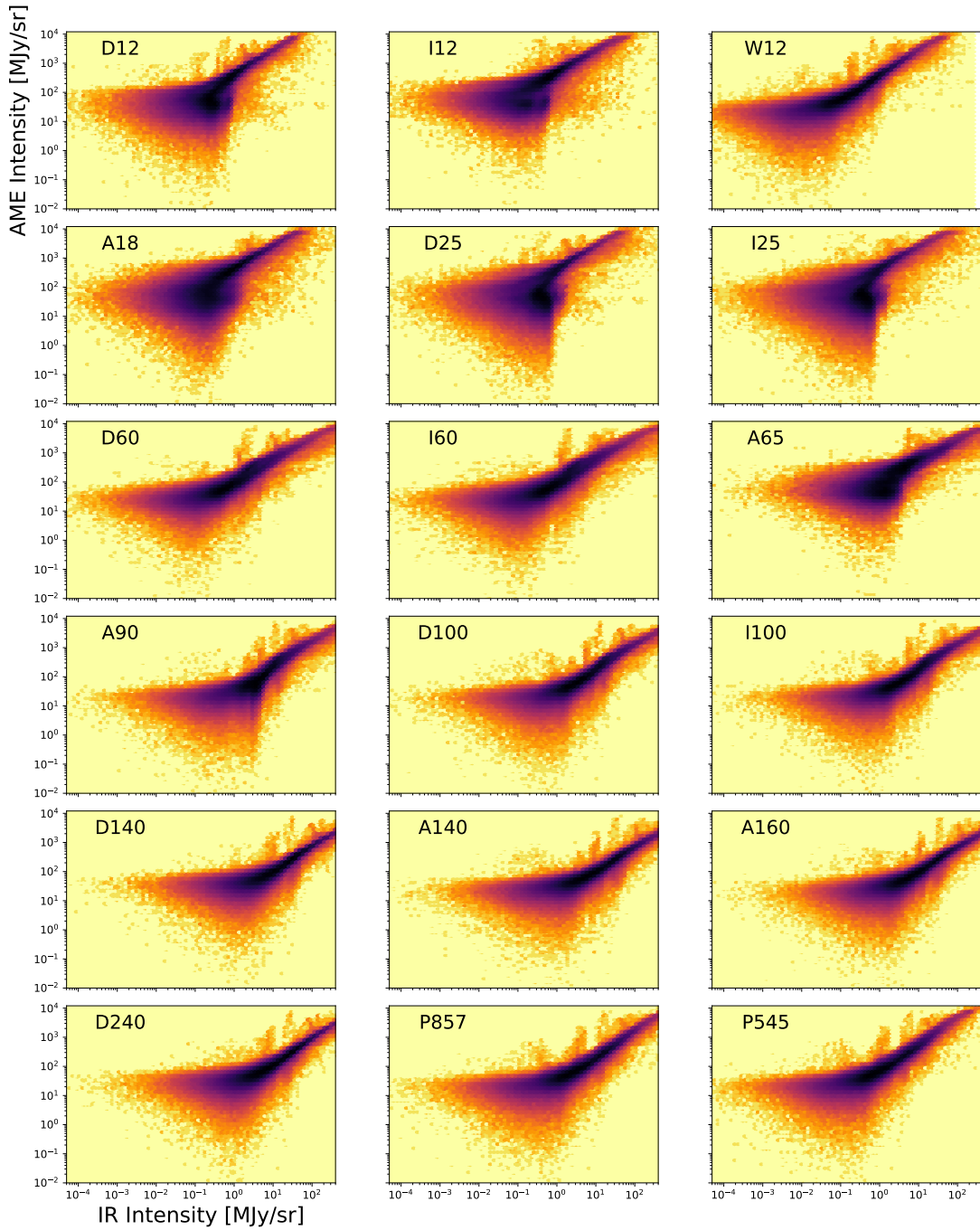


Fig. 5.— ALL-SKY plots of each of the 19 infrared bands' photometry results against those of the PR2 map. Similar to plots from the previous section, however these are produced on an all-sky basis. Cyan points represent pixels within 5 degrees of the galactic plane. Magenta points are pixels over 5 degrees from the galactic plane. Pixels within 5 degrees of the ecliptic plane are not plotted. Due to the large number of pixels plotted, a low alpha value is used (0.02). This helps to visualize the bulk of the pixels, but also means that portions of the plot with low point-density may seem blank on the page. Figure 3.1 shows the cross-correlation test results.

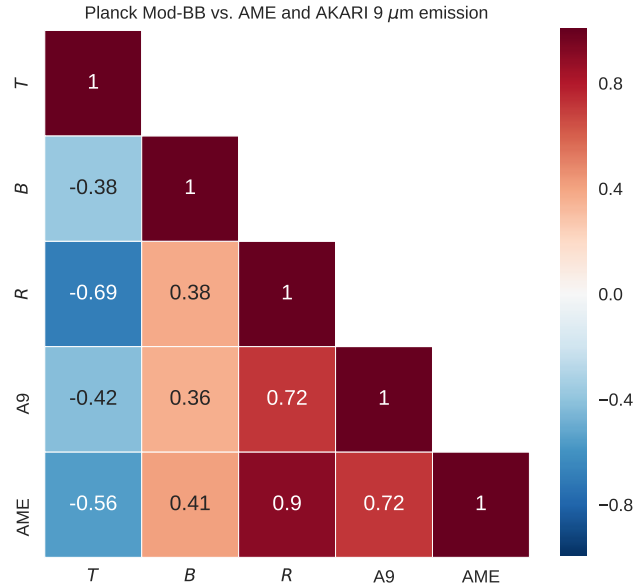


Fig. 6.— Spearman cross-correlation test (S) of AME vs. dust radiance (R), temperature (T), emissivity index (β), and the AKARI 9 μm brightness (A9), of the whole sky. Thermal dust parameters are provided in the Planck Coll. PR2 data. This provides a simplified picture of the AME vs. IR dust emission relationship. We can see that the results are consistent with the cross-correlation of AME vs. the 19 photometric intensities in Figure 3.1. This plot gives the results using the whole sky. Fig. ?? shows correlation results as they vary by GLAT and GLON.

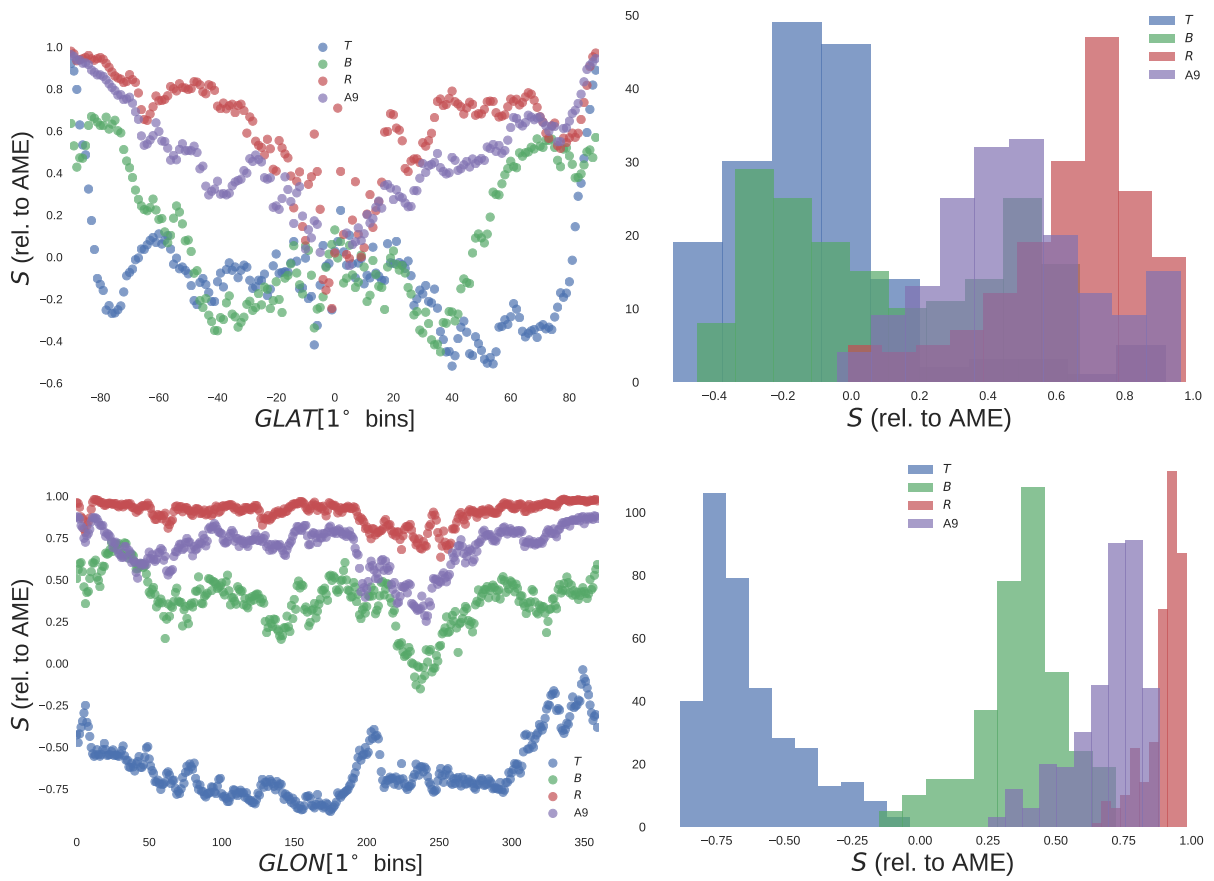


Fig. 7.— Top Left: Cross-correlation tests (Spearman) of AME vs. dust radiance (R), temperature (T), emissivity index (Beta), and the AKARI 9 μm brightness (A9), by b . Top Right: Histograms of the correlation scores. Bottom Left and Right: The same analysis repeated for galactic longitude.

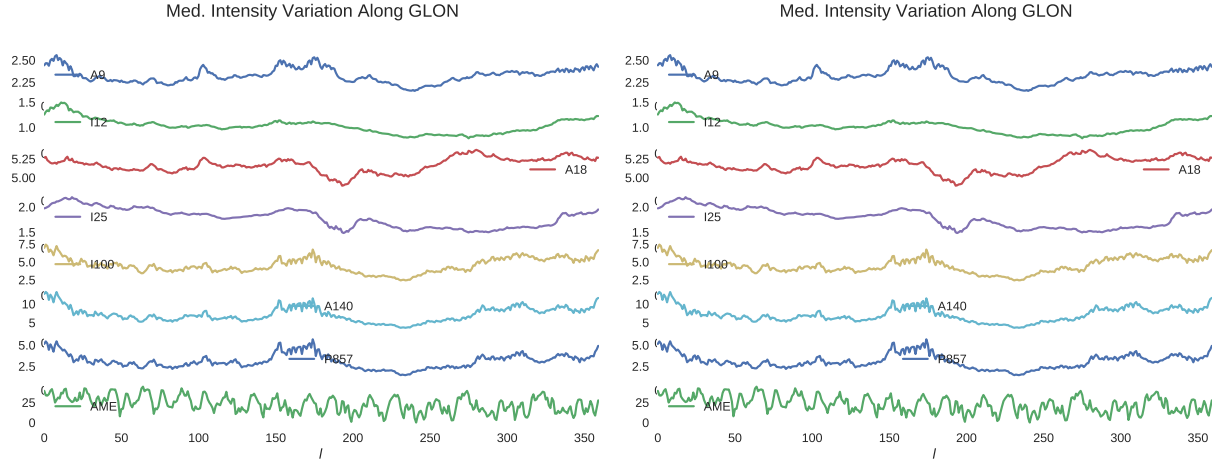


Fig. 8.— Top: Ratios of IR intensity to AME for 1-degree GLON bins (Left), and for GLAT bins (Right). Bottom: The same analysis as Top, but with the IR intensities being scaled by the AME.

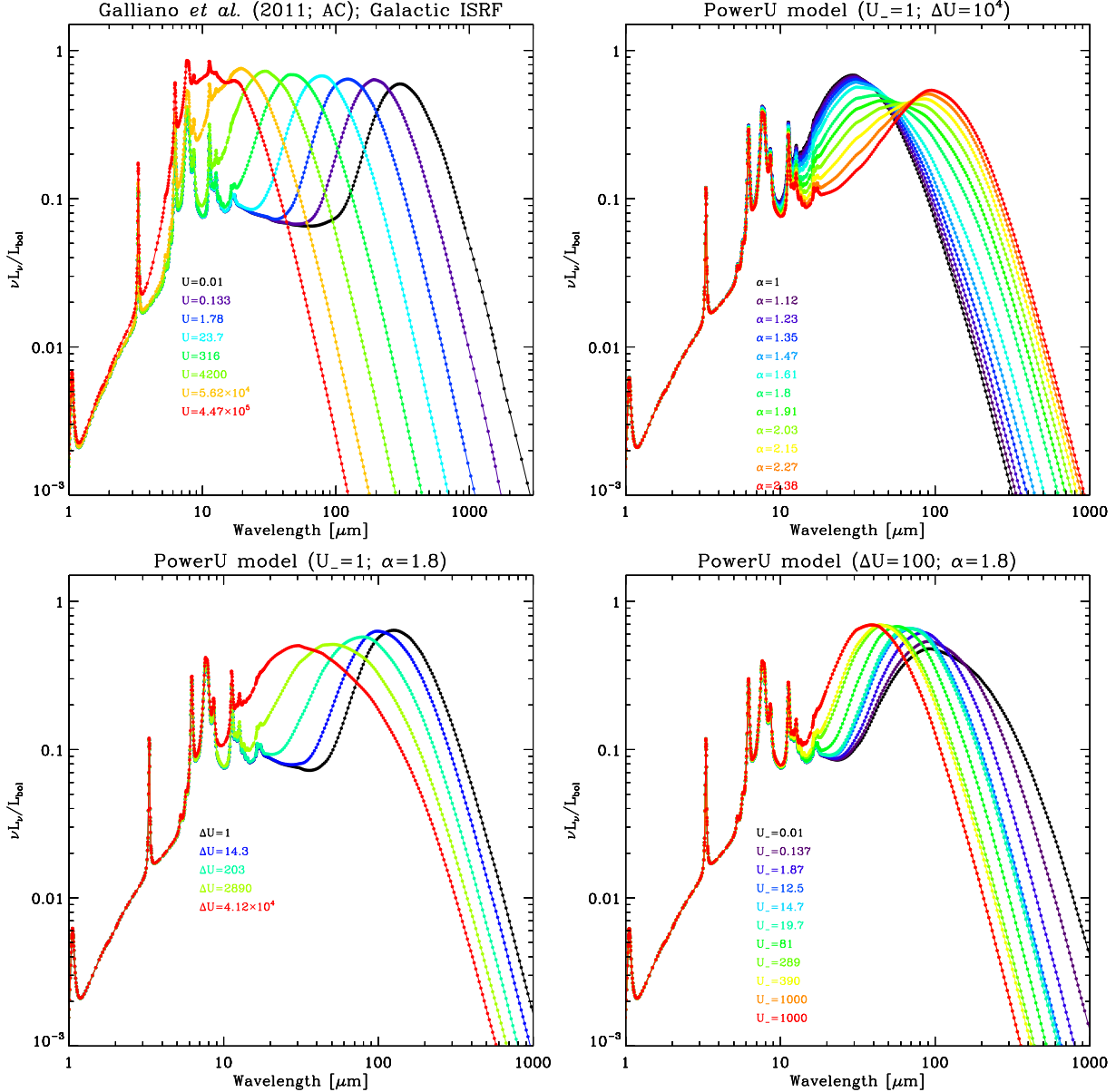


Fig. 9.— Dust templates of Galliano et al. (2011). The upper-left panel shows the variation of a uniformly illuminated mixture, as a function U . The other three panels show the variations of the emission of a dust mixture exposed to a distribution of starlight intensity, varying each parameter of Eq. 1.

the PCXV analysis (wherein component separation, of AME from known foregrounds, was done region-by-region.) Furthermore, the regions themselves are categorized as high (red circles) or low (blue circles) significance AME. Simply based on Figure 3.2, it is difficult to discern a difference on the correlation strengths.

To statistically evaluate the situation, we employ the Bootstrap re-sampling approach, first introduced by Efron (1979). This involves creating 100,000 random re-sampled sets of the data. We use the "with replacement" approach, meaning that a data point may be selected multiple times in a single re-sampling iteration. However the size of the re-sampled set is the same as the input set size. For each random set we run a correlation test, resulting in a distribution of correlation coefficients. The results of the Bootstrap analysis are given in Figure 3.2. The distributions of correlation coefficients for AME vs. PAH mass, and AME vs. total dust mass., appear to be distinct. Mean correlation coefficients are separated by $0.1+/-0.05-0.07$.

3.3. Analysis of the λ Orionis Region

Having looked at the AME vs. dust emission story on a very course scale, we now introduce our analysis of a particular region. The λ Orionis molecular ring, shown in Figure 3.3 as it appears in 1-degree smoothed AKARI 9 μm data, indicates excess microwave emission attributed to AME (Planck Collaboration et al. 2016b). At approx. 10 degrees wide, we can see the outline of the structure even in the low (1 degree FWHM) resolution Planck-COMMANDER AME map. This is one of the only structures on the sky with a relatively well-distinguished shape at such low resolution. In order to shift towards an investigation of individual AME-prominent regions, we have carried out an initial comparison of the AME of this region with its mid to far-IR dust emission.

Figure 3.3 shows how the region looks, for 12 different photometric bands, from the mid to far IR. The contours show the region's structure as given by the Planck PR2 AME map. Figure ?? shows simple IR to AME cross correlation plots, for all pixels within the 10 by 10 degree λ Orionis region. Our findings for lambda λ Orionis indicate an AME-PAH correlation, but we are unable to argue for a causal link.

4. Discussion

We have compared AME with infrared dust emission from 3 different approaches, however the results and discussion contained here apply to an angular scales of approximately 1-degree. In general, our results support an AME-from-dust hypothesis. At 1-degree angular resolution, we do not find evidence that the AME is exclusively carried by PAHs. The correlation of far IR dust emission with AME appears to be the best predictor, with MIR/PAH emission being marginally more weakly correlated with AME. In the case of lambda Orionis, AME vs. PAH is at least as strong as AME vs. FIR. Higher resolution studies will be needed in the future to fully solve the AME mystery.

4.1. AME:Dust

As noted in Section 1, previous studies found that the AME generally correlates at dust-related IR wavelengths (Ysard et al. 2010; Planck Collaboration et al. 2014c; Hensley et al. 2016). We see the same overall pattern in the present study, for each of the three scales examined: the all-sky pixel-based analysis, the re-examination of Planck AME Candidate regions, and the inspection of the λ Orionis region.

In our all-sky, pixel-by-pixel comparison, we find that all of the 19 wavelengths sampled show a first-order correlation with the AME. This is again consistent with the previous investigations of the AME cited above, wherein the only differences found are minor. Without applying further dust SED fitting, this analysis seems to concur with Hensley et al. (2016) in that the FIR bands (in their work, they used the dust radiance) show the tightest correlation with the AME.

In the case of the AME candidate regions, do we find evidence of a statistically stronger relationship between AME and total dust mass than AME vs. PAH mass, for the full set of 98 regions. We were able to confirm that the correlation coefficients are statistically distinct, via bootstrap re-sampling (with replacement.) However the difference is marginal. Moreover the full set of 98 regions includes many regions that are either near the galactic plane, or do not have a strong S/N for the AME component separation. A similar result is found when we compare AME to the total dust luminosity and PAH luminosity.

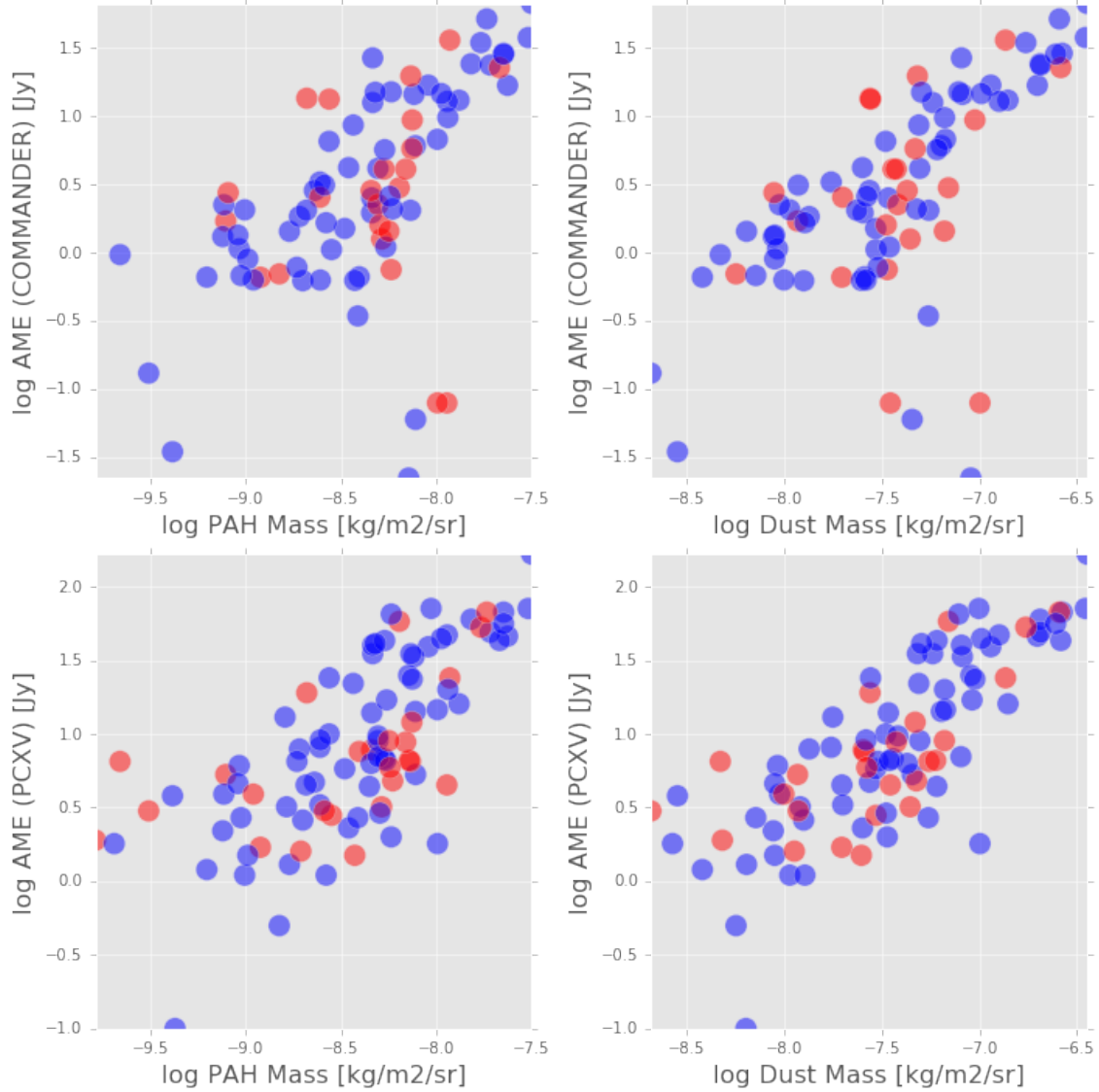


Fig. 10.— Results of circular aperture photometry and dust SED fitting for 98 regions listed in PCXV. Red dots indicated regions with significant AME. Blue dots indicated regions with low/zero significance AME.

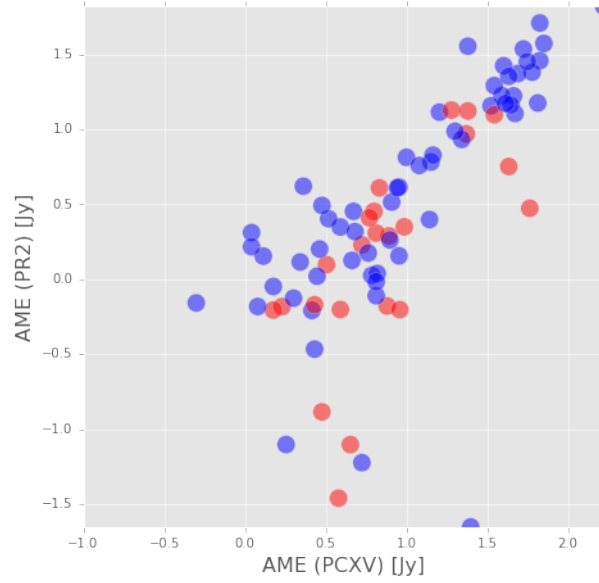


Fig. 11.— Left: Cross-comparison of the PCXV photometry results and the results of this work, based on the Planck Collaboration PR2 AME map.

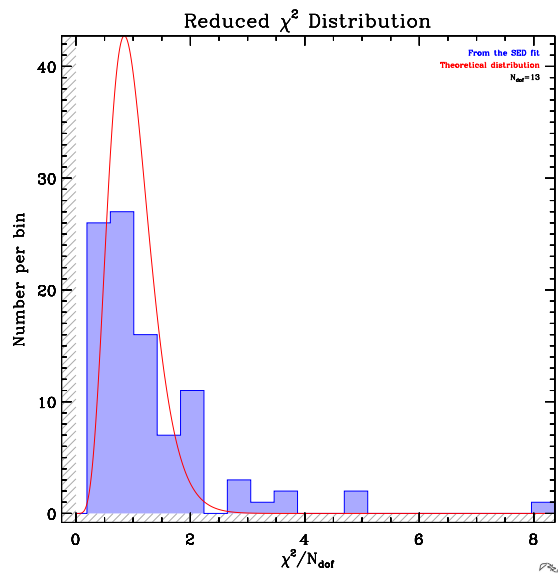


Fig. 12.— Histogram showing the χ^2 distribution of the dust SED fitting, to the AME region apertures.

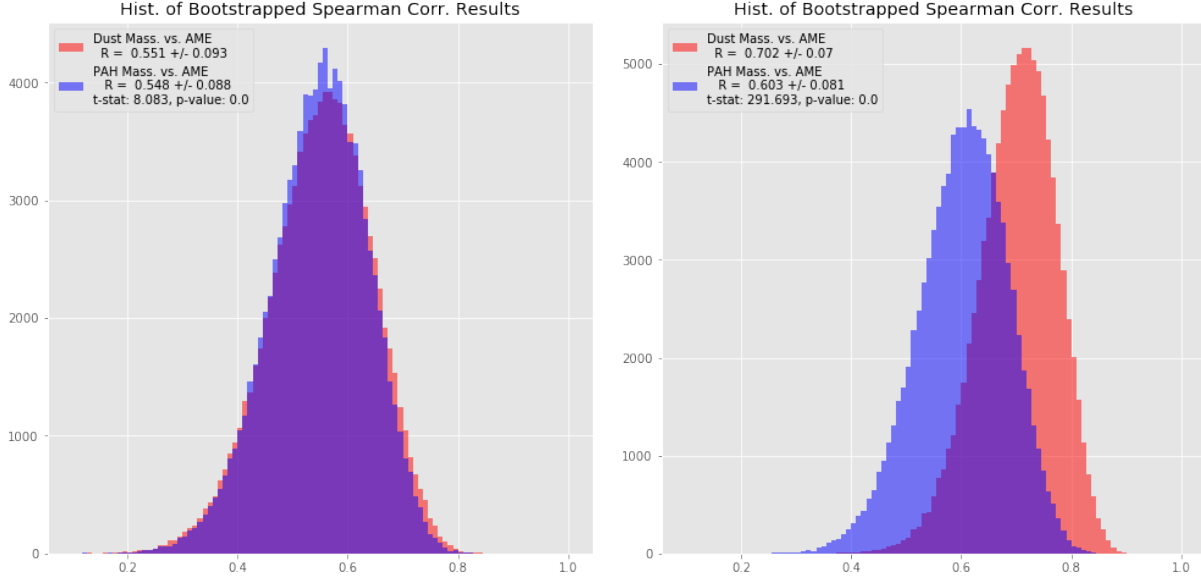


Fig. 13.— Left: Histogram showing the distribution of Spearman correlation test results (S), based on 100,000 Bootstrapped sub-samples for each of the two comparisons (AME vs. total dust mass and AME vs. PAH mass.), based on PCXV AME flux values of the full set of 98 candidate regions. Right: Same comparison repeated using fluxes obtained directly by circular aperture photometry on the PR2 map.

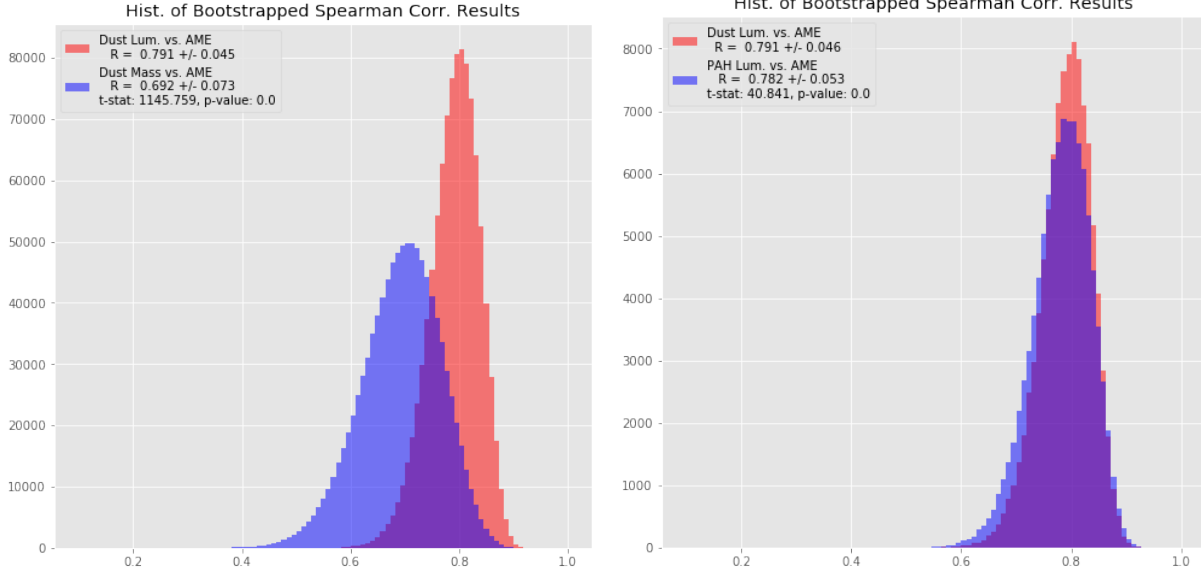


Fig. 14.— Left: Distribution of S results for AME vs. dust luminosity and AME vs. dust mass. Right: AME vs. dust luminosity and AME vs. PAH luminosity. The same Bootstrap comparison method as in Figure 3.2 is used.

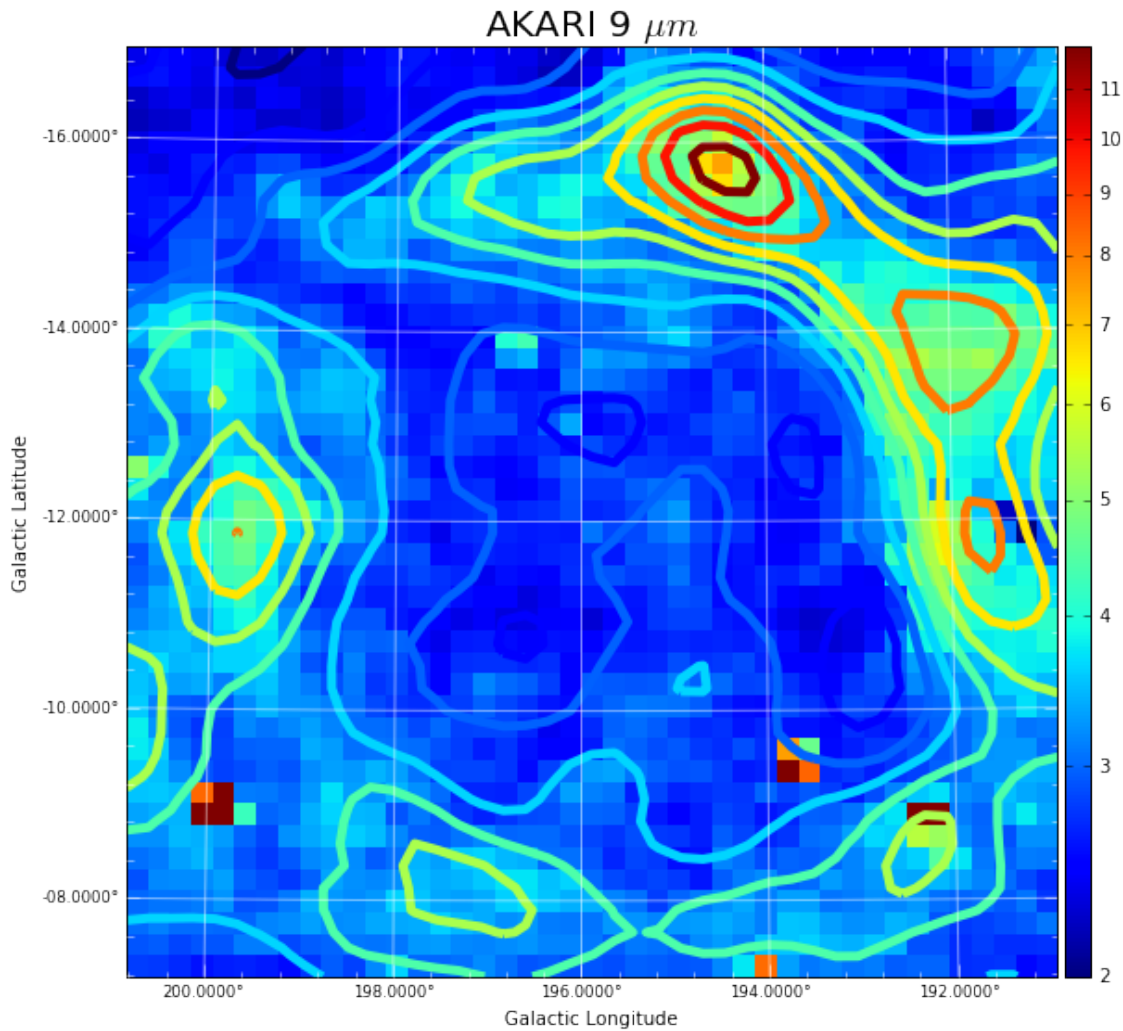


Fig. 15.— λ Orionis as it appears in the AKARI 9 μm data. Contours indicate the AME, as given by the Planck PR2 AME map. The image is smoothed to a 1-degree PSF (much larger than the original 10 arcsec map. The λ Orionis star itself is approximately located at the center of the image. The dust wave structure, described by *citation needed*, is apparent, and seems to coincide with a local maxima in the PR2 AME contours. The units are MJ/sr.)

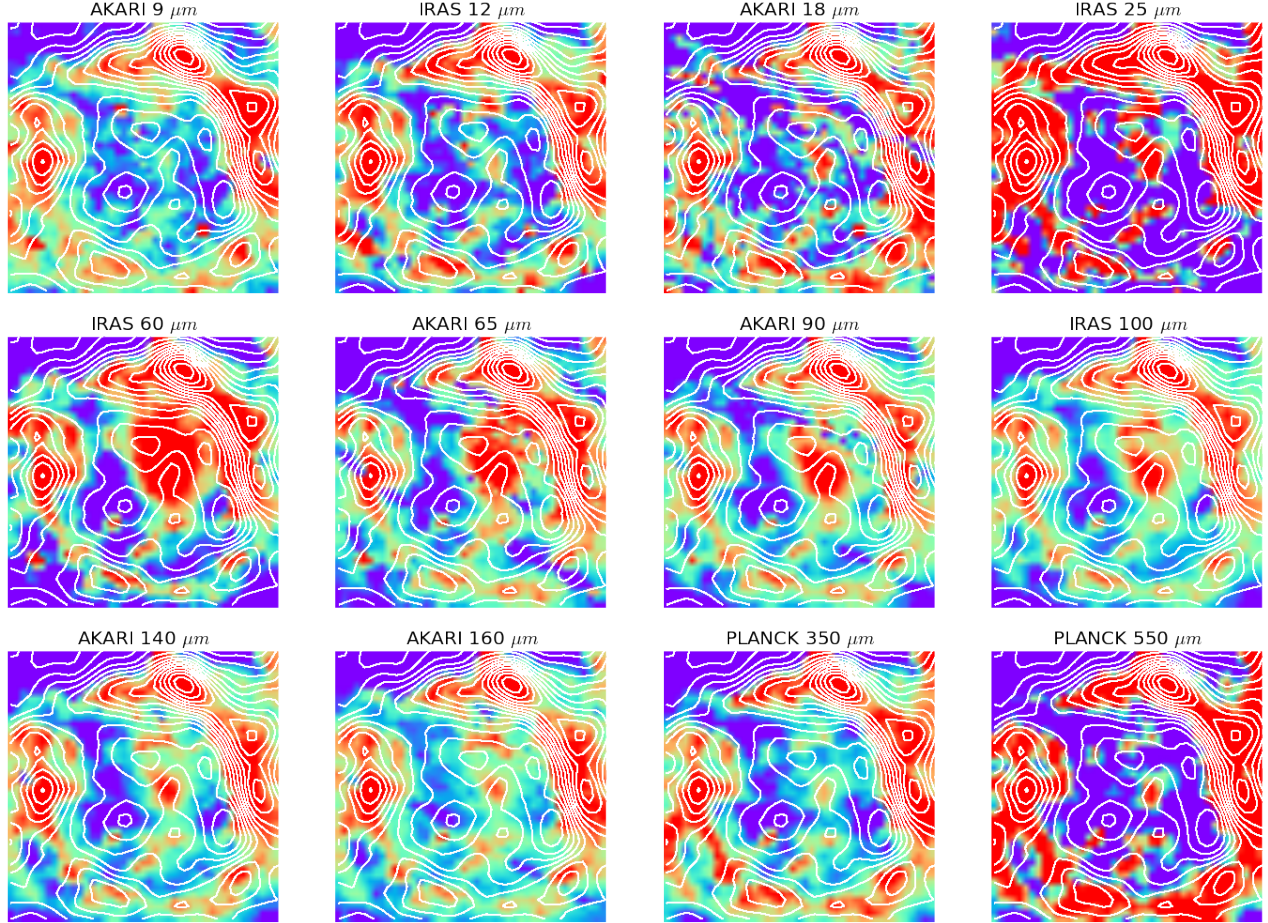


Fig. 16.— A grid of thumbnails showing the λ Orionis region's structure, at 12 wavelengths, along with AME contours (shown in white countours. Spatial correlation seems to be the best at the shortest and longest wavelengths (AKARI/IRC 9 μm and Planck/HFI 550 μm) .

The closeness of the correlation coefficients found here is consistent with the results of the IRAS vs. AME correlation test result from Planck Collaboration et al. (2014c). They found that the correlation coefficient among the 4 IRAS bands (12, 25, 60, and 100 μm) differ from one another only by about 5%, across the whole set of 98 regions. The trend of AKARI MIR and FIR data vs. the AME does not disagree with their IRAS comparison. This work adds that bands longer than IRAS 100 μm also correlate strongly with AME, especially the two Planck/HFI bands used.

4.2. AME:PAH

In the case of λ Orionis we did find that the AKARI 9 μm emission, and the longest wavelength Planck 545 GHz emission had the strongest Spearman coefficients (0.81 and 0.80.) The results may be consistent with a scenario in which PAH mass, cold dust, and the AME are all tightly correlated. Weaker correlation from 25 to 70 μm may indicate that AME is weaker in regions of warmer dust and stronger radiation fields. If we consider the 9 μm band to be a tracer of PAH emission, and Planck 545 Ghz band to be a tracer of thermal dust emission, the result is in-line with what we have seen in Ysard et al. (2010) and Hensley et al. (2016). In those works, the two relationships (MIR vs. AME and FIR vs. AME) are very close, although these two papers are odds as to which relationship is stronger, and thus in their final interpretation. However in the investigation of the Perseus molecular cloud complex by Tibbs et al. (2011), PAH emission (as well as VSG emission and hydrogen column density, N_H) does not show a strong correlation with AME compared to environmental paramters, such as dust temperature.

4.3. AME: T , G_0

According to spinning dust theory outlined in Draine & Lazarian (1998a) and in subsequent works by Ysard & Verstraete (2010), the AME profile and intensity will depend in part on the ISRF- but as is well-stated in Hensley & Draine (2017a), exactly how the ISRF will affect the AME SED is a more complicated question. Absorbed starlight photons may be able to rotationally excite the carriers, but if an enhanced ISRF leads to increased dust heating, then the increased IR emission can rotationally de-excite the carriers.

However the ISRF affects not only the dust temperature but ionization of the carriers. In our all-sky investigation, we find that the AME is anti-correlated with temperature with $S = -0.56$ on average. However we also find that this value varies between $S = -0.90$ and 0 along galactic meridians; between $S = 0$ and -0.6 along the parellels (Fig. 3.1). when looking at the Planck COMMANDER AME and thermal dust maps. Hensley et al. (2016) note a much weaker anti-correlation, $P = -0.06$ between AME dust temperature. However they scaled the AME by the dust radiance, and used a much more extensive pixel mask. In the context of a spinning PAH model, there is evidence that harder radiation fields are anti-correlated with PAH emission.

4.4. Microwave foreground component separation

There are also known degeneracies between the foreground parameters of the COMMANDER maps (spinning-dust, and free-free, synchrotron components as described in Planck Collaboration et al. (2016a).)

4.5. Summary

From these results, we cannot confirm or rule out a spinning-PAH hypothesis on an all-sky, 1-degree scale. While nanosilicates or magentic dipole emission from dust may be plausible contributors to the AME, as shown in Hoang et al. (2016); Hensley & Draine (2017a), we do not find (at least at resolutions considered here) that PAHs can be ruled-out as a carrier. While it is true that the FIR in our study has a tighter correlation with AME than PAH-related bands, the correlation with PAH emission remains. Either this is a coincidental correlation- PAHs and AME are both correlated with the “actual” carrier/s of AME, MIR photometric bands are not as good of a tracer of the actual PAH mass as we believed, or perhaps that PAHs are indeed contributing to the AME but that they are just one of multiple sources of the AME.

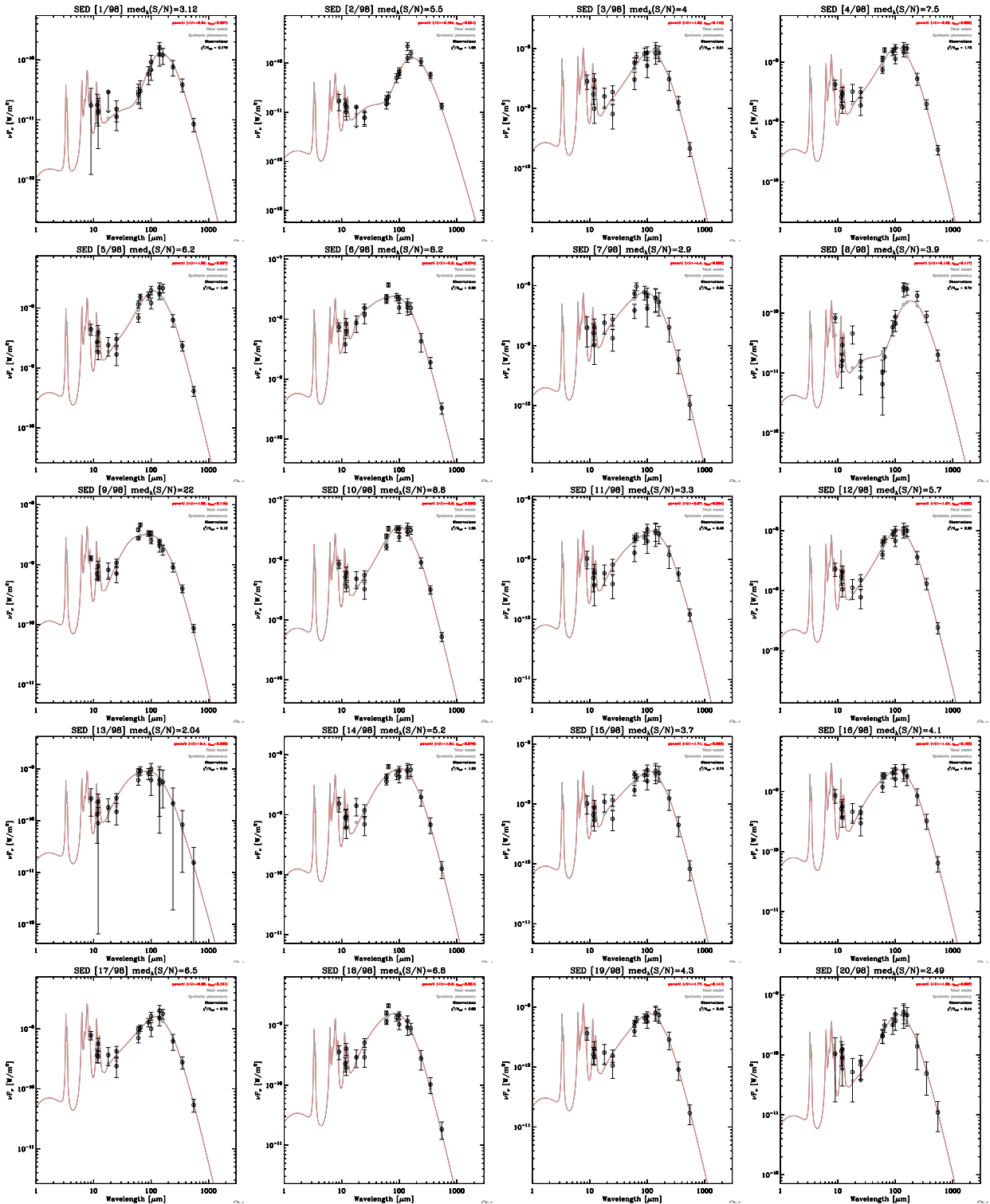
If it can be shown that IR emission from non-PAH small dust particles, such as nanosilicates strongly correlates with the AME, another very interesting question would need to be addressed: why does PAH emission *not* show a strong cor-

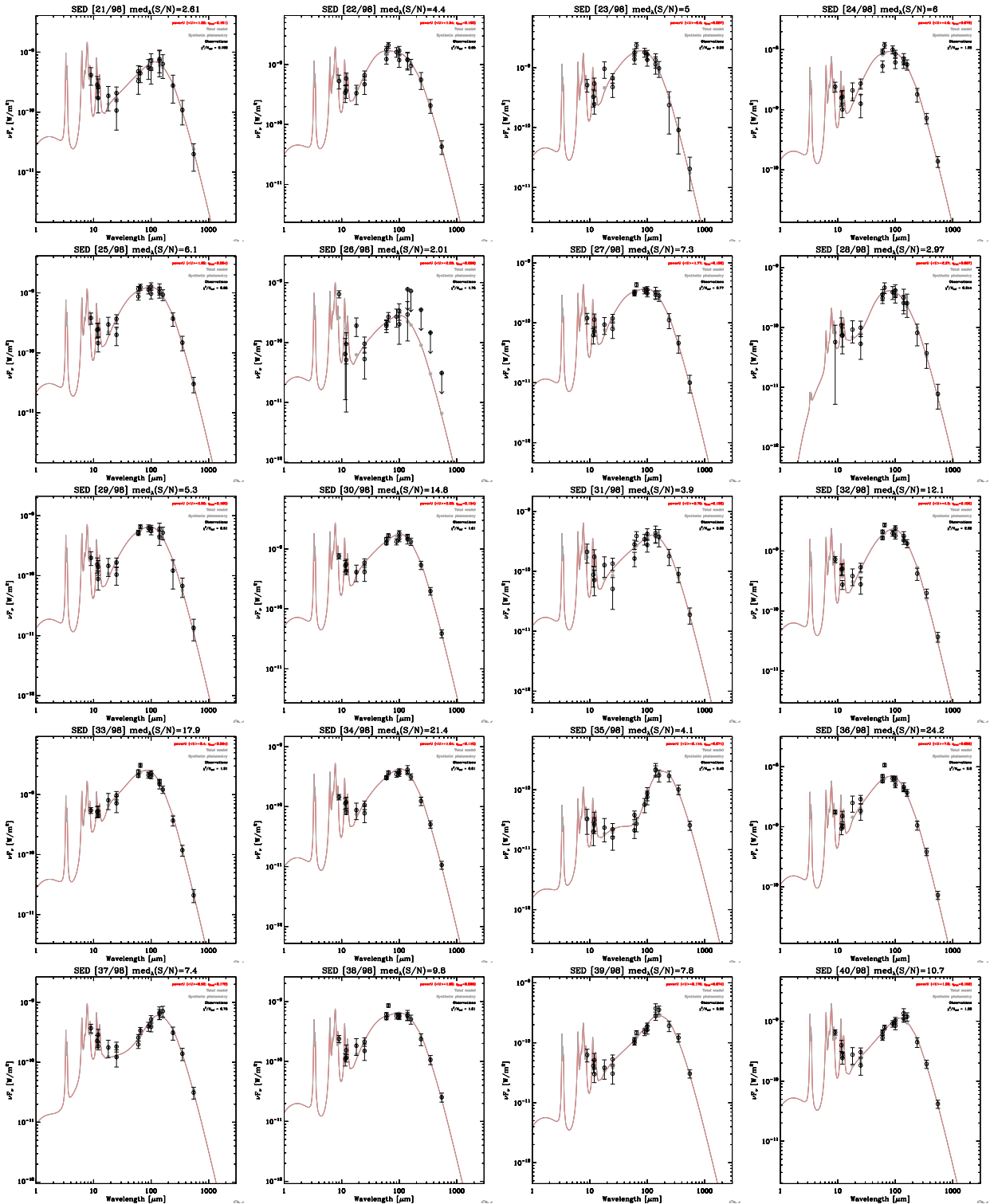
relation? Do PAHs not have the range of dipole moments needed to produce emission in the 10 - 90 GHz range? Because, as is described in Draine & Lazarian (1998a) and again in Hensley & Draine (2017b), such small particles should be spinning at the frequencies consistent with AME. Thus if we believe a particular class of small dust particles to exist, PAHs, nanosilicates, or otherwise- then they must be producing microwave emission, unless they do not have a permanent electric dipole.

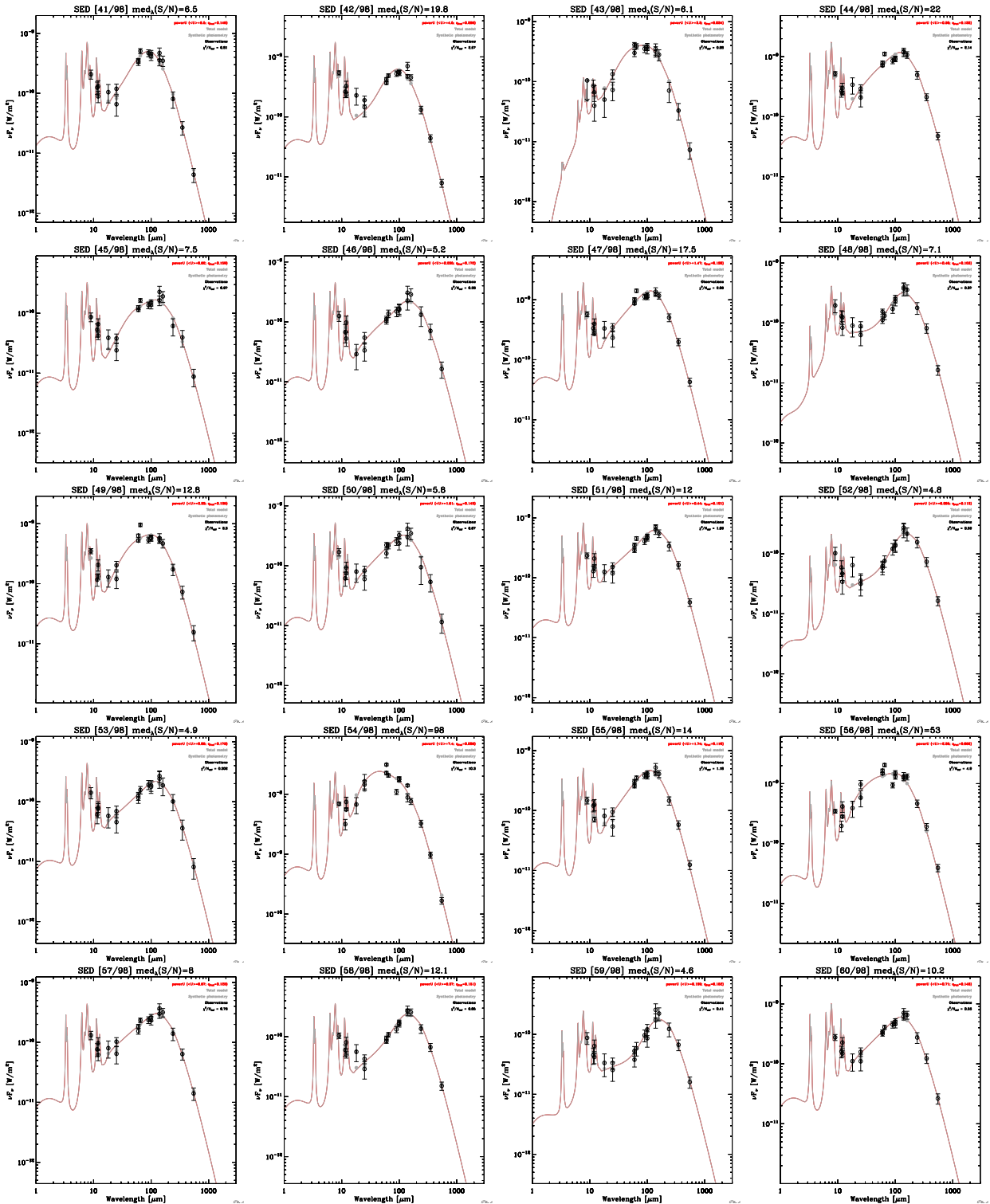
If there is a sufficient abundance of PAHs with an electric dipole, then we must consider the possibility that the data currently available to do not offer the necessary spatial resolution, or that the photometric bands used do not allow us to adequately separate the individual dust components (i.e. the PAH features from potential nanosilicate features) and/or microwave foreground emission components (free-free from spinning-dust.) We look forward to continued environment-resolved comparisons to investigate the potential AME-PAH (or AME-nanosilicates, iron nanoparticles) relationship in a region by region, especially given the disagreement we find between our examination of lambda Orionis and the all-sky analysis.

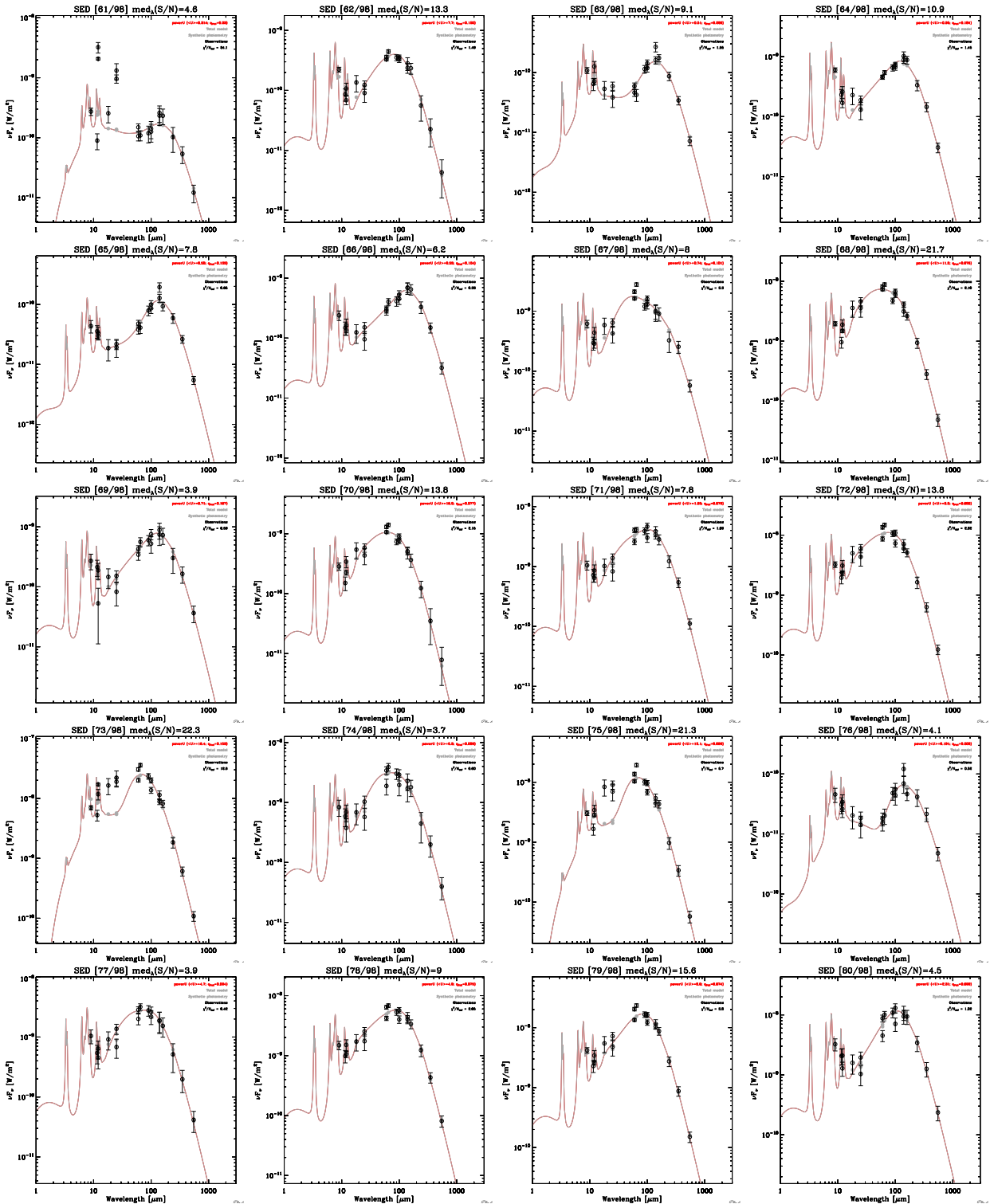
This project is supported by JSPS and CNRS under the Japan-France Research Cooperative Program. We would like to give special thanks to the AME Workshop 2016 attendees and organizer, Chris Tibbs, for enlightening discussions. Thanks also to Nathalie Ysard and Steven Gibson, and the staff of Grid, Inc. for helpful feedback.

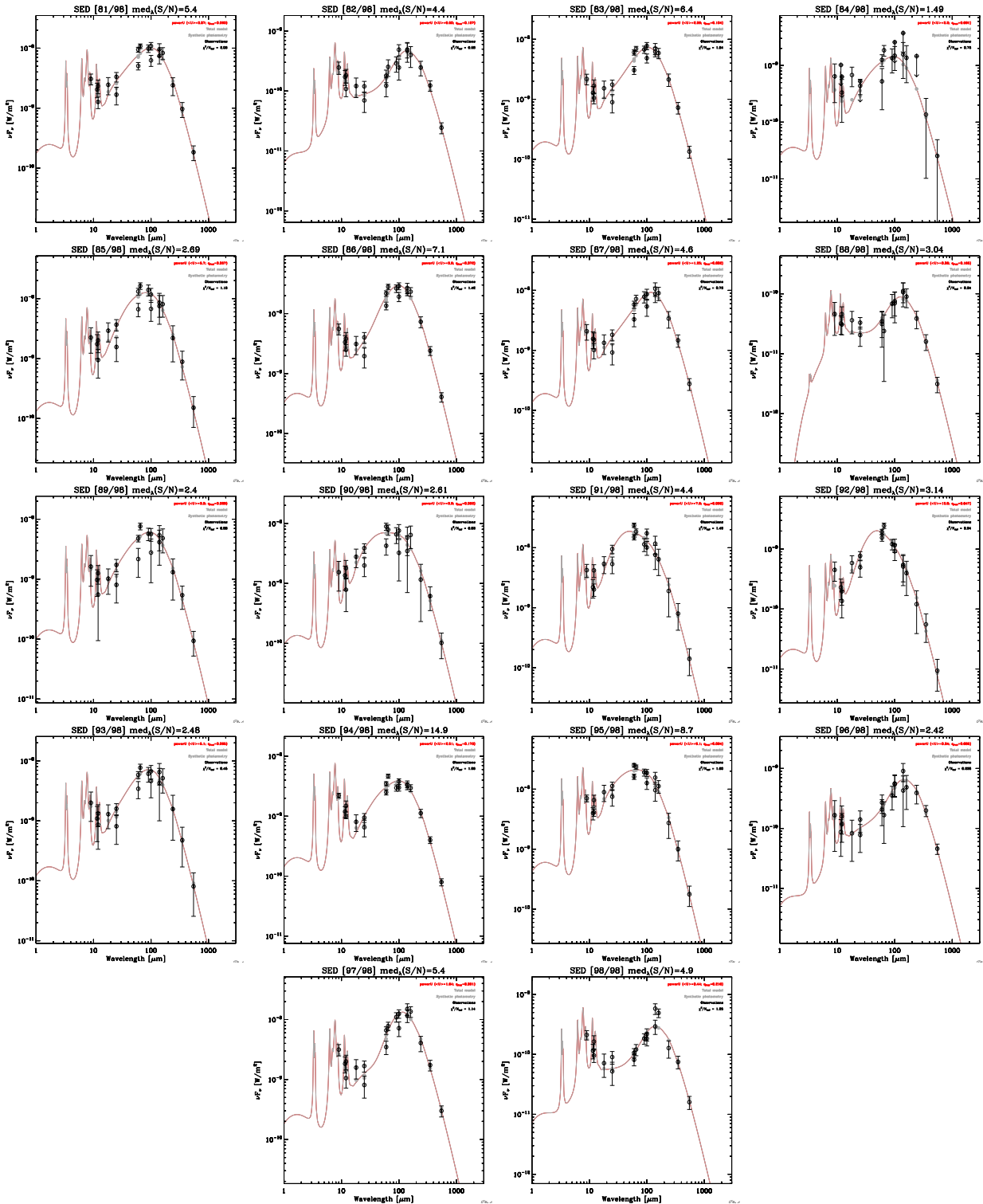
A. Appendix: SEDs











REFERENCES

- Ali-Haimoud, Y. 2010, SpDust/SpDust.2: Code to Calculate Spinning Dust Spectra, Astrophysics Source Code Library
- Ali-Haïmoud, Y. 2014, MNRAS, 437, 2728
- Ali-Haïmoud, Y., Hirata, C. M., & Dickinson, C. 2009, MNRAS, 395, 1055
- Andrews, H., Boersma, C., Werner, M. W., Livingston, J., Allamandola, L. J., & Tielens, A. G. G. M. 2015, ApJ, 807, 99
- Bonnarel, F., et al. 2000, A&AS, 143, 33
- Dale, D. A., Helou, G., Contursi, A., Silbermann, N. A., & Kolhatkar, S. 2001, ApJ, 549, 215
- de Oliveira-Costa, A., Kogut, A., Devlin, M. J., Netterfield, C. B., Page, L. A., & Wollack, E. J. 1997, ApJ, 482, L17
- Dickinson, C., Paladini, R., & Verstraete, L. 2013, Advances in Astronomy, 2013, 1
- Doi, Y., et al. 2015, PASJ, 67, 50
- Draine, B. T. 2011, Physics of the Interstellar and Intergalactic Medium
- Draine, B. T., & Hensley, B. 2013, ApJ, 765, 159
- Draine, B. T., & Lazarian, A. 1998a, ApJ, 494, L19
- . 1998b, ApJ, 508, 157
- . 1999, ApJ, 512, 740
- Draine, B. T., & Li, A. 2001, ApJ, 551, 807
- . 2007, ApJ, 657, 810
- Efron, B. 1979, Ann. Statist., 7, 1
- Erickson, W. C. 1957, ApJ, 126, 480
- Ferrara, A., & Dettmar, R.-J. 1994, ApJ, 427, 155
- Fioc, M., & Rocca-Volmerange, B. 1997, A&A, 326, 950
- Galliano, F., et al. 2011, A&A, 536, A88
- Giard, M., Lamarre, J. M., Pajot, F., & Serra, G. 1994, A&A, 286
- Górski, K. M., Hivon, E., Banday, A. J., Wandelt, B. D., Hansen, F. K., Reinecke, M., & Bartelmann, M. 2005, ApJ, 622, 759
- Hensley, B. S., & Draine, B. T. 2017a, ApJ, 836, 179
- . 2017b, ApJ, 834, 134
- Hensley, B. S., Draine, B. T., & Meisner, A. M. 2016, The Astrophysical Journal, 827, 45
- Hoang, T., Draine, B. T., & Lazarian, A. 2010, ApJ, 715, 1462
- Hoang, T., Vinh, N.-A., & Quynh Lan, N. 2016, ApJ, 824, 18
- Hoyle, F., & Wickramasinghe, N. C. 1970, Nature, 227, 473
- Ishihara, D., et al. 2010, A&A, 514, A1
- Jones, A. P. 2009, A&A, 506, 797
- Kawada, M., et al. 2007a, PASJ, 59, 389
- . 2007b, PASJ, 59, S389
- Kelsall, T., et al. 1998, ApJ, 508, 44
- Kogut, A., Banday, A. J., Bennett, C. L., Gorski, K. M., Hinshaw, G., & Reach, W. T. 1996, ApJ, 460, 1
- Kondo, T., et al. 2016, AJ, 151, 71
- Leitch, E. M. 1998, PhD thesis, CALIFORNIA INSTITUTE OF TECHNOLOGY
- Li, A., & Draine, B. T. 2001, ApJ, 554, 778
- Lovas, F. J., McMahon, R. J., Grabow, J.-U., Schnell, M., Mack, J., Scott, L. T., & Kuczkowski, R. L. 2005, Journal of the American Chemical Society, 127, 4345, pMID: 15783216
- Maddalena, R. J. 1986, PhD thesis, National Aeronautics and Space Administration. Goddard Inst. for Space Studies, New York, NY.
- Maddalena, R. J., & Morris, M. 1987, ApJ, 323, 179
- Mathis, J. S., Mezger, P. G., & Panagia, N. 1983, A&A, 128, 212
- Miville-Deschénes, M.-A., & Lagache, G. 2005, ApJS, 157, 302
- Murakami, H., et al. 2007, PASJ, 59, 369
- Neugebauer, G., et al. 1984, ApJ, 278, L1
- Onaka, T. 2000, Advances in Space Research, 25, 2167
- Onaka, T., Yamamura, I., Tanabe, T., Roellig, T. L., & Yuen, L. 1996, PASJ, 48, L59
- Onaka, T., et al. 2007, PASJ, 59, 401
- Planck Collaboration et al. 2014a, A&A, 571, A8
- . 2014b, A&A, 571, A12
- . 2014c, A&A, 565, A103
- . 2016a, A&A, 594, A10
- . 2016b, A&A, 594, A25
- . 2016c, A&A, 586, A132
- Takita, S., et al. 2015, PASJ, 67, 51
- Thorwirth, S., Theulé, P., Gottlieb, C. A., McCarthy, M. C., & Thaddeus, P. 2007, ApJ, 662, 1309
- Tibbs, C. T., et al. 2011, MNRAS, 418, 1889
- Ysard, N., Juvela, M., & Verstraete, L. 2011, A&A, 535, A89
- Ysard, N., Miville-Deschénes, M. A., & Verstraete, L. 2010, A&A, 509, L1
- Ysard, N., & Verstraete, L. 2010, A&A, 509, A12

